Solar Physics (2024) 299:112
https://doi.org/10.1007/s11207-024-02353-4

RESEARCH

Fabry-Pérot Interferometer Based Imaging Spectrometer for Fe I Line Observation and Line-of-Sight Velocity Measurement

Xingcheng Hu[1,2,3,4] · Jinsheng Yang[1,2] · Xuejun Rao[1,2] · Dingkang Tong[1,2] · Jiawen Yao[5] · Zhimao Du[5] · Qing Lin[5] · Changhui Rao[1,2,3]

Received: 29 January 2024 / Accepted: 24 July 2024 / Published online: 21 August 2024
© The Author(s), under exclusive licence to Springer Nature B.V. 2024

Abstract
High spectral resolution imaging spectroscopy plays a crucial role in solar observation, regularly serving as a backend instrument for solar telescopes. These instruments find direct application in deriving Doppler velocity from hyperspectral images, offering insights into the dynamic motion of matter on the solar surface. In this study, we present the development of a Fabry–Pérot interferometer (FPI) based imaging spectrometer operating at the Fe I (617.3 nm) wavelength for precise Doppler velocity measurements. The spectrometer features a moderate spectral resolution of $\lambda/\Delta\lambda \approx 60{,}000$, aiming to balance the imaging signal-to-noise ratio (SNR). The instrument underwent successful observational experiments on the 65-cm Educational Adaptive-Optics Solar Telescope (EAST) at the Shanghai Astronomy Museum. Obtained Doppler velocities were compared with data from the Helioseismic and Magnetic Imager (HMI), the maximum column and row correlation coefficients are 0.9261 and 0.9603, respectively. The estimated cut-off normalized frequency of the power spectral density (PSD) curve for velocity map is approximately 0.4/0.21 times higher than that observed in the HMI data, with potentially higher spatial resolution achievable under better seeing conditions. Based on the estimated imaging SNR levels, the accuracy of velocity measurements is approximately 50 m s^{-1}.

Keywords Doppler velocity · Spectrum · Fabry-Pérot interferometer

✉ C. Rao
chrao@ioe.ac.cn

1 National Laboratory on Adaptive Optics, Chengdu, Sichuan 610209, China

2 Institute of Optics and Electronics, Chinese Academy of Sciences, Chengdu, Sichuan 610209, China

3 University of Chinese Academy of Sciences, Beijing 100049, China

4 School of Electronic, Electrical and Communication Engineering, University of Chinese Academy of Sciences, Beijing 100049, China

5 Shanghai Astronomy Museum (branch of Shanghai Science & Technology Museum), Shanghai, China

1. Introduction

Doppler velocity, a key parameter in solar physics research, offers crucial insights into the motion of observed solar targets, contributing to our understanding of dynamic solar phenomena such as sunspots, flares, and filaments. The literature on the application of Doppler velocity in solar physics is extensive. Example references can be found in Rimmele and Marino (2006), Joshi et al. (2015), Yan et al. (2020).

Imaging spectroscopy with high spectral resolution, achieved through tunable narrowband filters such as Lyot–Öhmann filters and Fabry–Pérot interferometers (FPI), is essential for instrumental requirements. Such instruments are regularly integrated into both space solar telescopes, such as the Michelson Doppler Imager (MDI) for the Solar and Heliospheric Observatory (SOHO) (Scherrer et al. 1995), and the Helioseismic and Magnetic Imager (HMI) for the Solar Dynamics Observatory (SDO) (Pesnell, Thompson, and Chamberlin 2012; Scherrer et al. 2012), as well as ground-based solar telescopes, including the New Vacuum Solar Telescope (NVST) in China (Liu et al. 2014), the 1.5-m GREGOR solar telescope in Germany (Schmidt et al. 2012), the 1.6-m New Solar Telescope (NST) (Cao et al. 2010) at Big Bear Solar Observatory (BBSO), and the 4-m Daniel K. Inouye Solar Telescope (DKIST) at Hawaii (Schmidt et al. 2014). A detailed comparison of different types of instruments on such a topic can be found in Iglesias and Feller (2019).

In contrast to space-based solar telescopes, ground-based telescopes consistently feature larger apertures. However, the presence of atmospheric turbulence hinders them from achieving diffraction-limited imaging. Moreover, in the realm of time-sharing imaging spectroscopy, atmospheric turbulence can introduce additional spurious information. To address these challenges, the implementation of an Adaptive Optics (AO) system is a widely adopted strategy (Rimmele and Marino 2006; Rao et al. 2016; Zhang et al. 2023).

Among these instruments for imaging spectroscopy, FPI based narrowband imaging filters stand out for their narrower passbands and higher peak transmittance (Puschmann et al. 2012; Cavallini 2006; de la Cruz Rodríguez et al. 2015; Schmidt et al. 2014). These instruments usually use dual FPIs to significantly improve the free spectral range (FSR), but single FPI based instrument is also a good choice for simpler system design and less image degradation, such as the Visible Imaging Spectrometer (VIS) at the NST (Cao et al. 2010), which typically operates at 656.3 nm (Hα), 630.2 nm (Fe I), and 588.9 nm (Na), achieving a spectral resolution of $\lambda/\Delta\lambda \approx 85,000$.

The research presented in this paper builds upon our previous work involving the Narrow Band Imager (NBI) (Hu et al. 2022) which was tested at the 65-cm Educational Adaptive-Optics Solar Telescope (EAST) (Rao et al. 2022) located at the Shanghai Astronomy Museum. The NBI system initially employed a single FPI in conjunction with a prefilter to achieve narrow-band imaging at the Hα wavelength. In the current study, we have replaced the prefilter with a focus on the Fe I (617.3 nm) wavelength for Fe I line observation and line-of-sight (LOS) velocity measurement. The choice of this spectral line is primarily for two reasons: (i) it is the same line used in HMI, allowing us to use seeing-free observational data from HMI as a reference; (ii) this line is magnetically sensitive, and in the future, our instrument will be upgraded to include polarimetric capabilities for obtaining magnetic field information. The instrument underwent further testing at EAST, and this paper will provide detailed insights into the instrument configuration and the approach used for deriving LOS velocity.

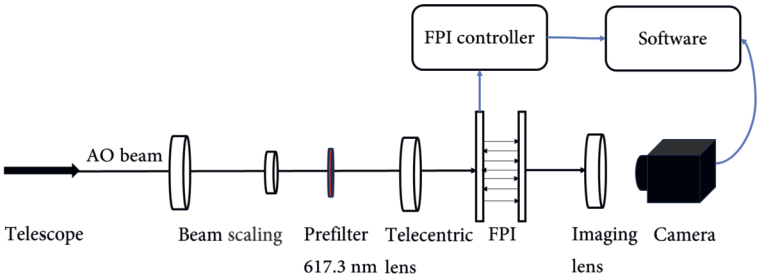

Figure 1 Schematic drawing of the instrument system.

Table 1 Specifications of the FP etalon.

Parameter	Value
Cavity length	562 μm
Range of cavity length adjustment	± 2.72 μm
Clear aperture diameter	104.96 mm
Surface flatness	λ/168 at 632.8 nm
FSR	0.356 nm at 632.8 nm
FWHM	0.00775 nm at 632.8 nm
Peak transmittance	82.2%

Table 2 Specifications of the prefilter.

Parameter	Value
Cavity	2
Center wavelength	617.38 nm
50% bandwidth	0.25 nm
10% bandwidth	0.48 nm
1% bandwidth	0.87 nm
Peak transmission	35.03%
Ambient temperature	23.0 °C

2. System Configuration

The primary system configuration remains unchanged from the description in Hu et al. (2022), and for readers' convenience, we briefly recapitulate it here. Figure 1 illustrates a schematic drawing of the system configuration. The specifications of our FPI (FP etalon, ET100) are outlined in Table 1, sourced from the etalon manufacturer, IC Optical Systems Ltd. The FPI is implemented in a telecentric mount to ensure consistent of the center wavelength for spectral transmission across the field of view (FOV) (Bailén, Orozco Suárez, and del Toro Iniesta 2023).

The prefilter is an interference filter manufactured by Andover Corporation, and its characteristics are depicted in Table 2.

3. Calibration of the System

3.1. Spectral Transmission Model

For the convenience of later discussions, we begin by establishing a spectral transmission model to represent the function of the instruments.

The primary components of the NBI system are the prefilter and the FPI etalon. For modeling a two-cavity interference filter (Löfdahl, Henriques, and Kiselman 2011), a double Airy function would theoretically be the correct choice. However, considering the non-ideality of the prefilter and the need for a simple fitting function for subsequent calibration procedures, we use the calibrated transmission data (normal incidence) to determine the appropriate fit. There are two basic types of functions that can be used to characterize the transmission function of a prefilter: the Gaussian function,

$$G(\lambda; \lambda_0, w_g, A) = A \exp\left(\frac{-4\ln 2(\lambda - \lambda_0)^2}{w_g^2}\right), \tag{1}$$

and the Lorentzian function,

$$L_p(\lambda; \lambda_0, w_l, B) = \frac{B}{1 + \left(2 \cdot \frac{\lambda - \lambda_0}{w_l}\right)^{2p}}, \tag{2}$$

where A and B represent the peak transmission, λ_0 denotes the center wavelength, w_g, w_l are the filter FWHM, and p is a parameter related to the cavity of the interference filter. To determine which function characterizes the prefilter better, four types of functions were examined to fit the measured transmission data: pure Gaussian function (G), pure Lorentzian function with $p = 2$ (L2), linear combination of Gaussian and Lorentzian function with $p = 1$ (G+L1), and a linear combination of Lorentzian functions with $p = 1$ and $p = 2$ (L1+L2). Figure 2 shows the fit results, indicating that it is better to use the L1+L2 type,

$$L(\lambda; \lambda_0, w_1, w_2, \eta, B) = B\left(\eta L_1(\lambda; \lambda_0, w_1) + (1 - \eta) L_2(\lambda; \lambda_0, w_2)\right), \tag{3}$$

to fit the prefilter, and when only the peak area is concerned, a single Gaussian fit is also sufficient.

The transmission function of the FPI etalon can be characterized as Airy's function (Beckers 1998),

$$h(\lambda, t) = \frac{1}{1 + \frac{4R}{(1-R)^2} \sin^2\left(\frac{2\pi\mu t \cos\theta}{\lambda}\right)}, \tag{4}$$

where R represents the reflectivity of the etalon surface, μ is the refractive index (for air-gap FPI etalon, $\mu = 1$), t is the FP cavity spacing, and θ is the angle of incidence.

Given the normalized Fraunhofer line profile $f(\lambda)$ and the continuum intensity I, the intensity detected by the CCD or CMOS camera can be expressed as

$$s = \int I f(\lambda) L(\lambda) h(\lambda, t) d\lambda. \tag{5}$$

The transmission peaks of $h(\lambda)$ shifts as the cavity spacing t is varied, and an intensity curve can be obtained by scanning across the line profile $f(\lambda)$,

$$s(\lambda) = (I f(\lambda) L(\lambda)) * h(\lambda), \tag{6}$$

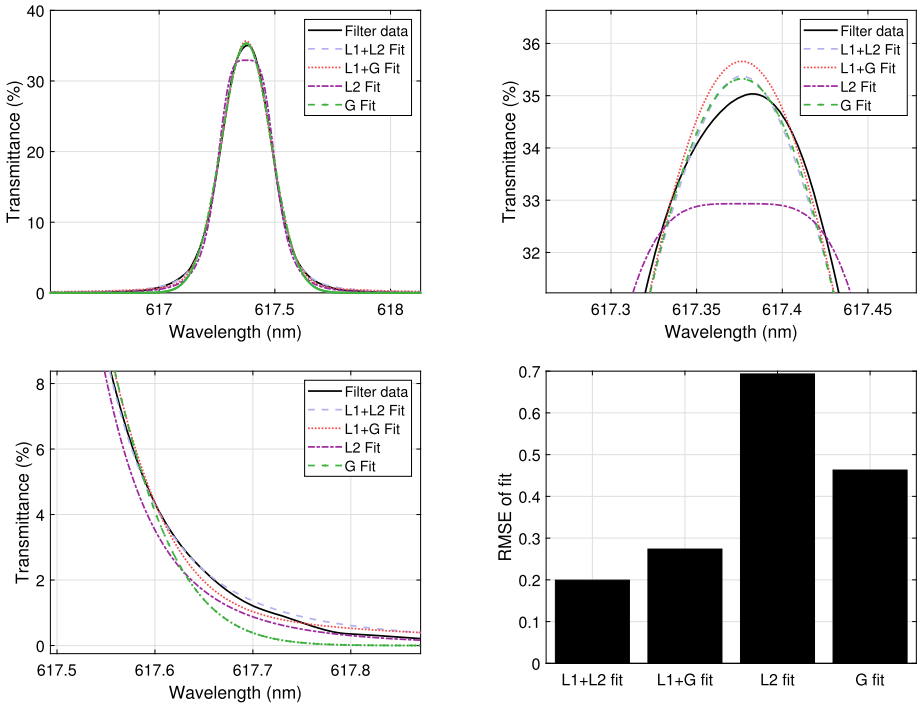

Figure 2 (Upper left) Fitting the measured transmission data of a prefilter using four different types of functions. (Upper right) Zoomed-in view of the peak area from the figure in the upper left. (Lower left) Zoomed-in view of the foot area from the figure in the upper left. (Lower right) Comparison of the root-mean-square-error (RMSE) among the different fits.

where $*$ stands for linear convolution.

3.2. Model Parameter Fit

The theoretical intensity curve $s(\lambda)$ in Equation 6 is determined by both the observational line profile and the parameters of the NBI system. A patch of the quiet region at the center of the solar disk can be selected to provide spectral signals for calibration, and the model parameters are solved by optimizing the nonlinear least squares problem

$$\hat{\mathbb{X}} = \min_{\mathbb{X}} \|s'(\lambda) - s(\lambda; \mathbb{X})\|_2, \tag{7}$$

where $\hat{\mathbb{X}}$ represents the optimal parameters set to be determined, $s'(\lambda)$ is the observed intensities, and $s(\lambda; \mathbb{X})$ is generated by passing the atlas spectrum through the spectral transmission model.

The left panel of Figure 3 displays the experimentally observed intensity curve $s(\lambda)$ alongside the theoretical curve generated by the spectral transmission model with the optimal set of model parameters; the model fits well with the observed intensities. The line profile after prefilter correction is displayed; however, due to the slightly wide FWHM of the FPI, the deconvolution of the line profile encounters numerical issues, and thus, these specific results are not presented. The right panel illustrates the transmission profiles of

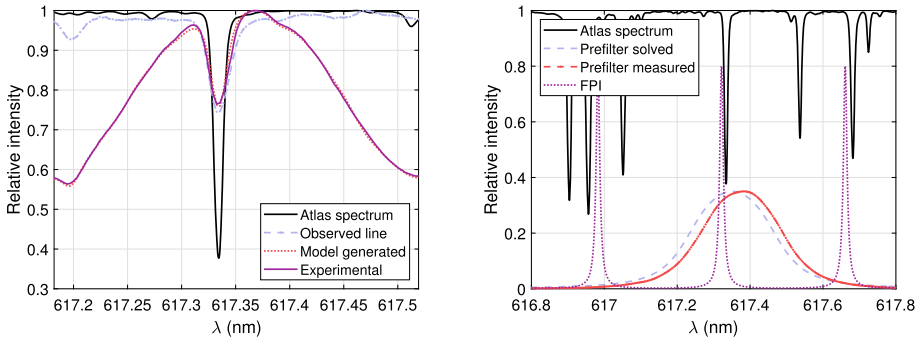

Figure 3 (Left) The experimental intensity curve $s(\lambda)$ (in purple) corresponding to the theoretical curve $s'(\lambda)$ generated by the spectral transmission model with the optimal model parameter set (in red), a line profile by correcting the prefilter (in blue), and the atlas Fe I line profile (in black); (Right) The transmission profile of the calibrated NBI system, including prefilter transmission (in blue) and FPI transmission (in purple), the red line showing the prefilter transmission data measured by the manufacturer, and the black line indicating the atlas spectrum.

Table 3 Calibrated parameter values.

Parameters	R	Δd (μm)	w_1 (nm)	w_2 (nm)	η	λ_0 (nm)
Mean	0.899	1.37	0.198	0.274	0.365	617.357
Std.	0.007	0.01	0.027	0.019	0.032	0.010

the prefilter and FPI etalon. Upon comparison with manufacturer-measured data, the solved transmission profile of the prefilter exhibits a slight blue shift. Ten independent calibration experiments were conducted successively within a total duration of approximately 30 minutes, the calibrated model parameters are listed in Table 3.

4. Doppler Velocity Derivation

4.1. Sampling Configuration

The Doppler velocity can be derived from the hyperspectral images obtained as the FPI scans across the Fe I line. Optimal sampling parameters are essential for balancing noise reduction and time efficiency. Therefore, it is crucial to discuss the sampling configuration, including the scan range and sampling frequency. Given that only a convoluted line profile is observable, first the 617.3 nm atlas spectrum is convoluted with the FPI transmissions. To establish the appropriate scan range, it is advisable to consider a velocity range spanning from -5 km s^{-1} to $+5$ km s^{-1}, which corresponds to typical LOS velocities observed on photosphere (the photospheric sound speed is about 10 km s^{-1}). The convoluted atlas line profiles are shifted by the corresponding wavelengths. As shown in Figure 4, a threshold (99%) is employed to identify the sampling window that requires coverage. Beyond this window, the sampling intensity becomes insensitive to the Doppler shift, making it unnecessary to include those regions.

The sampling frequency can be determined using the Nyquist–Shannon sampling theorem. By applying a Gaussian fit to the convoluted atlas line, the FWHM w of the profile

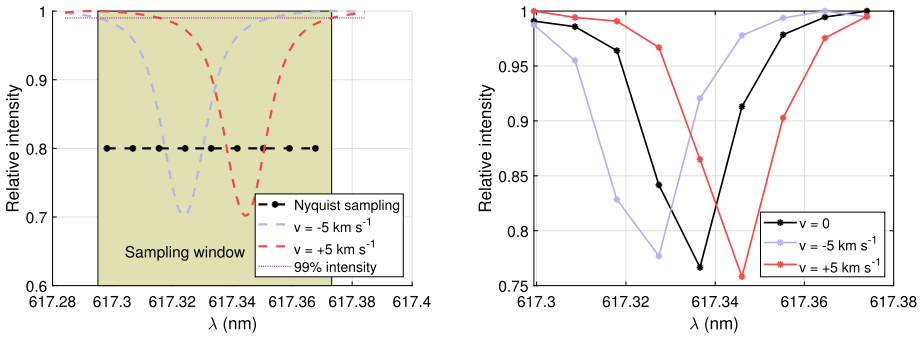

Figure 4 (Left) The sample window need to be covered and the Nyquist sampling points; (Right) The scan intensities obtained by passing the shifted atlas spectrum to the instrumental transmissions, the asymmetry of these intensities is corrected with the prefilter transmission.

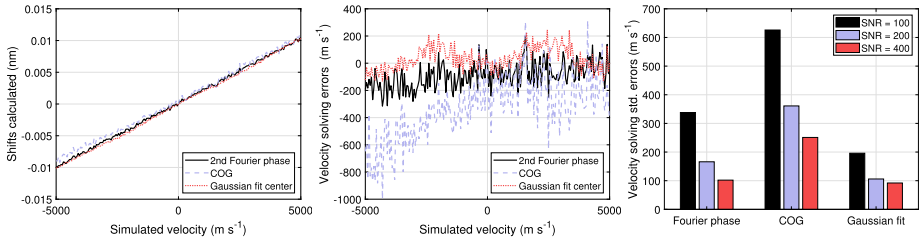

Figure 5 (Left) The wavelength shifts calculated from the scan intensities (SNR = 400) using three different methods; (Middle) The corresponding velocity errors; (Right) Standard deviation of the calculated results compared between these methods under different SNR conditions.

can be estimated. The Nyquist sampling frequency can be approximated to $0.5w$, as illustrated in Figure 4. Based on this analysis, our instrument should scan at least nine sample points along the 617 nm Fe I line. For FPIs with narrower transmission peaks, the sampling window could be narrower, necessitating an improvement in the sampling rate.

4.2. Simulations

Numerical simulations were conducted to validate the procedures for deriving Doppler velocities. The 617.3 nm atlas spectrum was Doppler shifted by velocities ranging from -5 km s^{-1} to $+5$ km s^{-1}. Subsequently, it was passed through the spectral transmission model of our instrument, and noise was modeled as photon noise following a Poisson distribution. The sampling configuration is defined as described in Section 4.1 and the spectral transmission model is characterized as described in Section 3.

To derive Doppler velocities from the scan intensities, three methods are used: the center of gravity (COG), the second-order Fourier phase (Jones 1989), and the center of Gaussian fit (Couvidat et al. 2012). These three methods are implemented to calculate the wavelength shifts, which are expected to be linearly related to the Doppler velocities. The simulation results are shown in Figure 5.

The simulation results indicate that the COG method performs the worst with our instrument, while the Gaussian fit method is the most robust to noise. However, one drawback of the Gaussian fit method is the computational cost associated with calculating least squares.

In good signal-to-noise ratio (SNR) conditions, the Fourier phase method achieves nearly the same performance as the Gaussian fit method but is faster, making it the preferred choice currently.

4.3. Observational Experiment and Data Processing

4.3.1. Observations

The instrument underwent testing at the EAST on November 3, 2023. The observation target chosen was the active sunspot region NOAA 13477, expected to exhibit abundant dynamic motion patterns. Initially, the calibration procedure described in Section 3 was performed to map the digital cavity spacing encoding of the FPI to absolute wavelength values. Based on the calibration results and the sampling configuration analyzed in Section 4.1, the scan configuration of the FPI was set up with some redundant coverage and sampling rate (typically 28 samples). The exposure time was set to 20 frames $\times$ 20 ms, allowing a complete scan to be conducted within 1 minute. Scientific images at each spectrum sample point were captured with the AO system closed-loop, while flat-field images were acquired by defocusing and continuously changing the pointing of the telescope within an FOV of about 5 arcminutes. The observational images underwent dark current and flat-field correction, deconvolution using the point spread function (PSF) of the imaging system, and correlation shift addition among multiple frames. Finally, images at different wavelengths were meticulously aligned using a subimage cross-correlation method.

4.3.2. Fabry-Pérot Interferometer Correction

FPI based narrowband images require additional correction for transmission inhomogeneity across the FOV. Despite our FPI being designed with a telecentric configuration to mitigate blue shifts from nonvertical incidence angles, nonideal features arising from manufacturing—including nonuniform cavity spacing and plate reflectivity—cause variations in filter transmissions (passband center and FWHM) among pixels within the same scan step. This variability introduces noticeable artifacts into the images (de la Cruz Rodríguez et al. 2015). Furthermore, for Doppler shift measurements, the cavity errors of the FPI contribute significant errors because the wavelength coordinates of intensity samples depend heavily on the FOV. Consider the pixel dependent form of Equation 6,

$$s(\lambda, x, y) = (I(x, y) f(\lambda, x, y) P F(\lambda)) * h(\lambda, x, y), \tag{8}$$

where

$$h(\lambda, x, y) = \frac{1}{1 + \frac{4R(x,y)}{(1-R(x,y))^2} \sin^2\left(\frac{2\pi\mu t(x,y)\cos\theta}{\lambda}\right)}. \tag{9}$$

In Equation 8, the prefilter is considered to be pixel-independent. Although the prefilter is placed in a collimated beam and potentially having defects, some blue shifts should exist according to the FOV, since the prefilter transmission is much broader than FPI's, such effects can be reasonably neglected.

The term $h(\lambda, x, y)$ can be solved for by applying the calibration technique described in Equation 7 to each pixel of the scanned flat-field images, for which the continuum and line profile are supposed to be uniform:

$$I(x, y) f(\lambda, x, y) = I_0 f_0(\lambda). \tag{10}$$

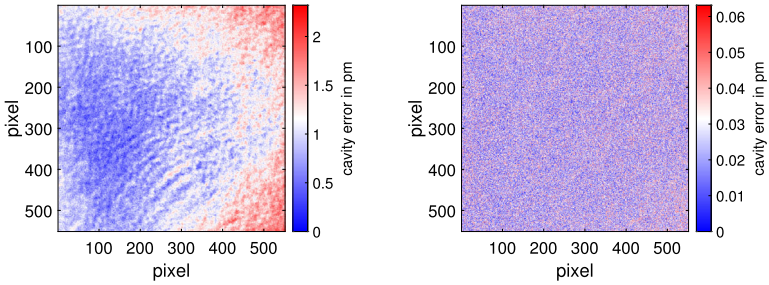

Figure 6 (Left) The original cavity-error map (RMS = 0.311 pm); (Right) The corrected cavity-error map (RMS = 0.012 pm).

Unfortunately, even though $h(\lambda, x, y)$ can be accurately determined, for our instrument, the FWHM of FPI is too wide to deconvolve with the observed intensities, thus $s(\lambda, x, y)$ cannot be recovered by Equation 8.

Instead, a reference pixel can be chosen, and its transmissions is used to "format" other pixels. First, a series of correction filters are generated using the flat-field images:

$$s_0(\lambda, x, y) = (I_0 f_0 P F(\lambda)) * h(\lambda, x, y) = (I_0 f_0(\lambda) P F(\lambda)) * h_{\mathrm{ref}}(\lambda) * \Delta h(\lambda, x, y), \quad (11)$$

$$\Delta H^{-1}(x, y) = \frac{\mathcal{F}_\lambda \{s_0(\lambda, x_{\mathrm{ref}}, y_{\mathrm{ref}})\}}{\mathcal{F}_\lambda \{s_0(\lambda, x, y)\}}, \quad (12)$$

where $\mathcal{F}_\lambda$ denotes Fourier transformation in the wavelength dimension. Then these filters can be applied to scientific images:

$$s'(\lambda, x, y) = \mathcal{F}_\lambda^{-1} \left\{ \mathcal{F}_\lambda \{s(\lambda, x, y)\} \cdot \Delta H^{-1}(x, y) \right\}. \quad (13)$$

After such a correction, all pixels share the reference pixel's FPI transmission. When correcting only for cavity errors, $\Delta H^{-1}(x, y)$ can be a simple phase filter. The following method is adopted: the relative line shift among the pixels of the flat-field images is first calculated using their Fourier phase. Then, for each pixel, its line profile is interpolated and shifted according to the cavity-error map. This process is implemented iteratively until the root mean square (RMS) of the cavity-error map reaches a satisfactory level. Figure 6 illustrates the original cavity-error map and the corrected cavity-error map. In the left panel, the wavelength shift across the FOV is estimated using flat-field images, with an RMS value of 0.311 pm corresponding to a Doppler velocity of 150 m s^{-1}. By aligning the line profile of each pixel, this value is reduced to 0.012 pm, as shown in the right panel, corresponding to a Doppler velocity of 6 m s^{-1}, which is reasonable for Doppler velocities measured from flat-field images. Once the cavity-error map has been corrected, a global shift map is obtained. This shift map can then be applied to correct both the flat-field and scientific images. In Figure 7, we illustrate the impact of the cavity-error and its correction. Without cavity-error correction, there is a noticeable artificial intensity distribution contributing to the image. Although in the same scan step, some pixels with a smaller cavity spacing measure the wing intensities of the spectral lines, others with a larger cavity spacing measure the core intensities, resulting in darker regions. Such effects are effectively eliminated after the correction procedure.

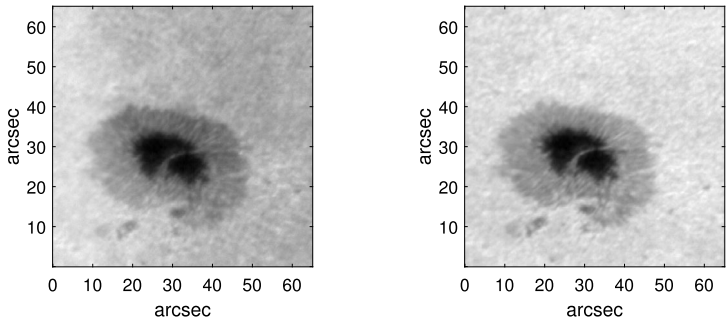

Figure 7 (Left) Image (about 6 pm from line center) processed without cavity-error correction; (Right) The same image but processed with cavity-error correction.

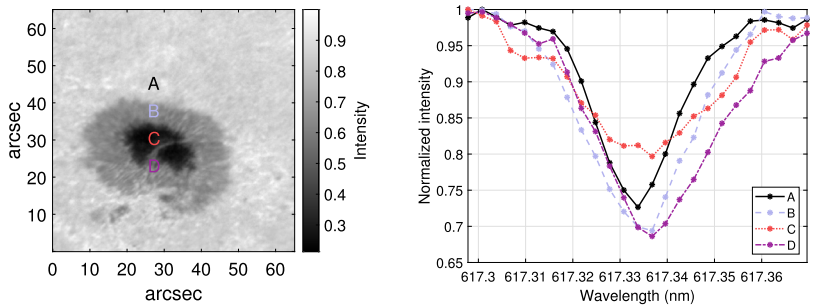

Figure 8 (Left) Intensity image at line center; (Right) Spectrum line profiles of the corresponding pixels that marked in the line center intensity image.

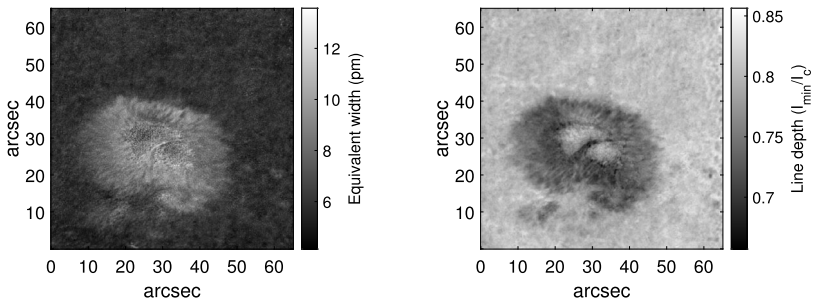

Figure 9 Spectrum line equivalent width (left) and depth (right).

4.4. Doppler Velocity Results

Once the image processing procedures have been executed, the Doppler velocity can be calculated. Figure 8 presents the intensity image at the Fe I line center along with the spectrum line profiles of the corresponding pixels marked in the line center intensity image. 2D maps of the equivalent width and line depth estimates are presented in Figure 9.

The Doppler velocity map is calculated as described in Section 4.2. Simultaneous observational data from HMI were also obtained. In Figures 10 and 11, our observational data

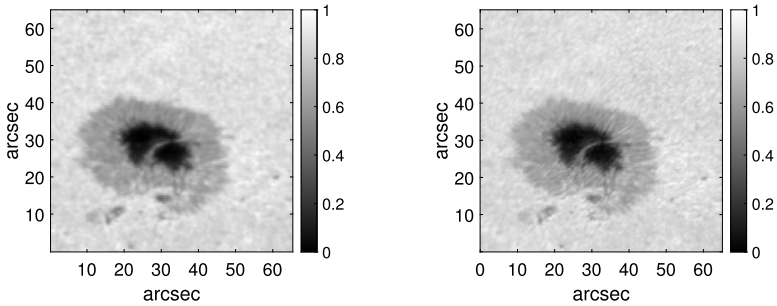

Figure 10 Cotemporal and cospatial continuum intensity image (NOAA 13477, November 3, 2023, 04:23:15 UTC) comparison between the HMI's (left) and ours (right).

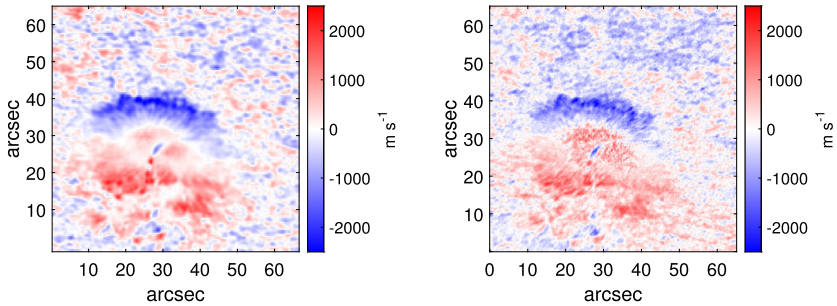

Figure 11 Cotemporal and cospatial LOS velocity map comparison between the HMI's (left) and ours (right).

is aligned with HMI's data after image rotation and correlation matching. The comparison results indicate that our observational Doppler velocity is consistent with HMI's, although our data is still influenced by seeing effects.

4.5. Performance Evaluation

4.5.1. Correlation with HMI Data

To evaluate the performance of the instrument, the column and row cross-correlations between HMI's velocity map and ours (resampled to the same resolution) are calculated. The area exhibiting the maximum correlation is in the sunspot region, where it is best corrected by the AO system. Specifically, the maximum column and row correlations are 0.9261 and 0.9603, respectively. In comparison, for the continuum intensity map, these values are notably higher at 0.9983 and 0.9975. This suggests that while our velocity measurements exhibit consistency with the seeing-free HMI data, there remains a considerable gap between the velocity and intensity measurements.

4.5.2. Spatial Resolution

To evaluate the spatial resolution of the observational results, the power spectral density (PSD) of the velocity maps is calculated (radial averaged), as shown in Figure 12. The cut-off frequency is estimated to be the frequency at -5 dB decay. This comparison indicates

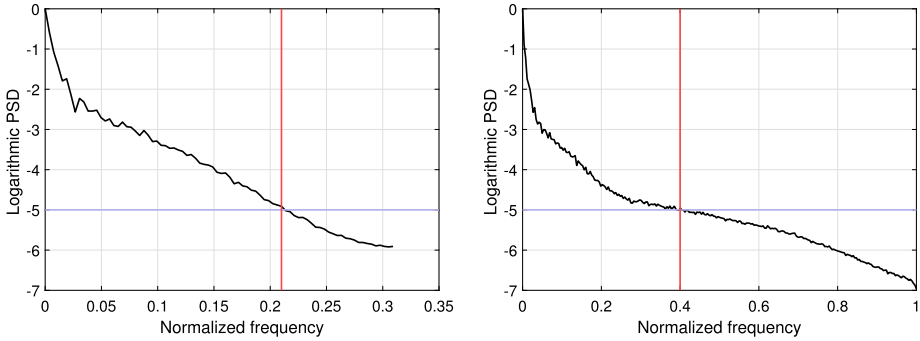

Figure 12 PSD curve of HMI's velocity map (left, $f_{\text{cut-off}} \approx 0.21$) and PSD curve of the velocity map observed by our instrument (right, $f_{\text{cut-off}} \approx 0.40$). The spatial frequency is normalized to half of the sample frequency (0.26″) of our data, which is approximate to the diffraction limit of a 65-cm telescope at 617 nm (0.24″).

that the spatial resolution of our observational velocity map is higher than that of the HMI data (note that the aperture of HMI telescope is approximately 14 cm), but it is still far from reaching the diffraction limit.

4.5.3. Accuracy Estimation

The accuracy of LOS velocity measurements is related to the SNR level, which is determined by the exposure and scan configuration. The above observation uses the QHY4040 scientific CMOS camera (Zhang et al. 2020), according to the test data from the vendor and the camera configuration for this instance, the read out noise and system gain of the camera are estimated to be $3 \sim 14$ e^- and 0.43 e^-/ADU for 16 bit data, respectively. The average ADU level of the continuum image is about 20,000, resulting in a photon noise of about 90 e^- per frame, allowing us to neglect the readout noise. By averaging 20 frames, the SNR of the continuum image is about 400. The observational experiment sampled more points than the minimal requirement analyzed in Section 4.1, thus achieving higher accuracy. We ran the same simulation procedure as in Section 4.1 but with the actual experimental configuration, and the results indicate the standard deviation error for velocities ranging from -5 km s^{-1} to $+5$ km s^{-1} is about 50 m s^{-1}.

5. Summary and Future Work

This article provides a concise overview of the configuration of our FPI-based imaging spectrometer designed for observing the Fe I line. It outlines the calibration process and details the data processing procedure. Currently, the instrument primarily focuses on Doppler velocity measurement, with plans for several upgrades:

Moving to a Magnetic Insensitive Line for LOS Velocity Measurements: The Fe I 617.3 nm line is sensitive to magnetic fields, which may affected the accuracy of Doppler shift measurements, particularly in the sunspot umbra regions. In contrast, the Fe I 709.0 nm line is more suitable for pure velocity measurements due to its magnetic insensitive ($g = 0$), clean continuum, and better seeing.

Introduction of Polarization Analyzer Module: Integrating a polarization analyzer module into the instrument will transform it into a spectropolarimeter. This enhancement will enable the acquisition of vector magnetic field information from the Sun.

Installation on the 1.8-m CLST: The instrument is slated for installation on the 1.8-m CLST (Rao et al. 2020), which boasts a larger aperture and features a more robust AO system compared to the EAST. This relocation is anticipated to result in a remarkable improvement in image resolution.

Acknowledgments This work was supported by the National Natural Science Foundation of China (Grant Nos. 11727805 11703029 11733005 12103057 and 12261131508), and also funded by Shanghai Science & Technology Museum, Shanghai, China.

Author contributions Xingcheng Hu played a pivotal role in this research, spearheading the experimental plan, meticulously collecting and processing observation data, and crafting the main manuscript text. Jin-Sheng Yang contributed significantly by designing the imaging optical system, while Dingkang Tong skillfully assembled it. Jiawen Yao and Zhimao Du provided invaluable assistance during the observational experiment. Qing Lin played a crucial role in arranging and coordinating necessary resources. Supervision and manuscript review were expertly handled by Xuejun Rao and Changhui Rao.

Data Availability No datasets were generated or analysed during the current study.

Declarations

Competing interests The authors declare no competing interests.

References

Bailén, F.J., Orozco Suárez, D., del Toro Iniesta, J.C.: 2023, Fabry-Pérot etalons in solar astronomy. A review. *Astrophys. Space Sci.* **368**, 55. DOI. ADS.

Beckers, J.M.: 1998, On the effect of narrow-band filters on the diffraction limited resolution of astronomical telescopes. *Astron. Astrophys. Suppl. Ser.* **129**, 191. DOI. ADS.

Cao, W., Gorceix, N., Coulter, R., Ahn, K., Rimmele, T.R., Goode, P.R.: 2010, Scientific instrumentation for the 1.6 m New Solar Telescope in Big Bear. *Astron. Nachr.* **331**, 636. DOI. ADS.

Cavallini, F.: 2006, IBIS: a new post-focus instrument for solar imaging spectroscopy. *Solar Phys.* **236**, 415. DOI. ADS.

Couvidat, S., Rajaguru, S.P., Wachter, R., Sankarasubramanian, K., Schou, J., Scherrer, P.H.: 2012, Line-of-sight observables algorithms for the Helioseismic and Magnetic Imager (HMI) Instrument tested with Interferometric Bidimensional Spectrometer (IBIS) observations. *Solar Phys.* **278**, 217. DOI. ADS.

de la Cruz Rodríguez, J., Löfdahl, M.G., Sütterlin, P., Hillberg, T., Rouppe van der Voort, L.: 2015, CRISPRED: a data pipeline for the CRISP imaging spectropolarimeter. *Astron. Astrophys.* **573**, A40. DOI.

Hu, X., Yang, J., Rao, X., Rao, C.: 2022, Fabry-Pérot interferometer-based tunable narrow-band imager for solar chromospheric observation: First results. *Solar Phys.* **297**, 74. DOI. ADS.

Iglesias, F.A., Feller, A.: 2019, Instrumentation for solar spectropolarimetry: state of the art and prospects. *Opt. Eng.* **58**, 082417. DOI. ADS.

Jones, H.P.: 1989, Formation of Fourier phase shifts in the solar Ni I 6768 Å line. *Solar Phys.* **120**, 211. DOI. ADS.

Joshi, A.D., Forbes, T.G., Park, S.-H., Cho, K.-S.: 2015, A trio of confined flares in AR 11087. *Astrophys. J.* **798**, 97. DOI. ADS.

Liu, Z., Xu, J., Gu, B.-Z., Wang, S., You, J.-Q., Shen, L.-X., Lu, R.-W., Jin, Z.-Y., Chen, L.-F., Lou, K., Li, Z., Liu, G.-Q., Xu, Z., Rao, C.-H., Hu, Q.-Q., Li, R.-F., Fu, H.-W., Wang, F., Bao, M.-X., Wu, M.-C., Zhang, B.-R.: 2014, New vacuum solar telescope and observations with high resolution. *Res. Astron. Astrophys.* **14**, 705. DOI. ADS.

Löfdahl, M.G., Henriques, V.M.J., Kiselman, D.: 2011, A tilted interference filter in a converging beam. *Astron. Astrophys.* **533**, A82. DOI.

Pesnell, W.D., Thompson, B.J., Chamberlin, P.C.: 2012, The Solar Dynamics Observatory (SDO). *Solar Phys.* **275**, 3. DOI. ADS.

Puschmann, K.G., Denker, C., Kneer, F., Al Erdogan, N., Balthasar, H., Bauer, S.M., Beck, C., Bello González, N., Collados, M., Hahn, T., Hirzberger, J., Hofmann, A., Louis, R.E., Nicklas, H., Okunev, O., Martínez Pillet, V., Popow, E., Seelemann, T., Volkmer, R., Wittmann, A.D., Woche, M.: 2012, The GREGOR Fabry-Pérot interferometer. *Astron. Nachr.* **333**, 880. DOI. ADS.

Rao, C., Zhu, L., Rao, X., Zhang, L., Bao, H., Kong, L., Guo, Y., Zhong, L., Ma, X., Li, M., Wang, C., Zhang, X., Fan, X., Chen, D., Feng, Z., Gu, N., Liu, Y.: 2016, Instrument description and performance evaluation of a high-order adaptive optics system for the 1 m New Vacuum Solar Telescope at Fuxian Solar Observatory. *Astrophys. J.* **833**, 210. DOI. ADS.

Rao, C., Gu, N., Rao, X., Li, C., Zhang, L., Huang, J., Kong, L., Zhang, M., Cheng, Y., Pu, Y., Bao, H., Guo, Y., Liu, Y., Yang, J., Zhong, L., Wang, C., Fang, K., Zhang, X., Chen, D., Wang, C., Fan, X., Yan, Z., Chen, K., Wei, X., Zhu, L., Liu, H., Wan, Y., Xian, H., Ma, W.: 2020, First light of the 1.8-m solar telescope-CLST. *Sci. China Phys. Mech. Astron.* **63**, 109631. DOI. ADS.

Rao, C., Rao, X., Du, Z., Bao, H., Li, C., Huang, J., Guo, Y., Zhong, L., Lin, Q., Ge, X., Yang, J., Fan, X., Liu, Y., Jia, D., Li, X., Li, M., Zhang, M., Cheng, Y., Zhou, J., Yao, J., Zhang, L., Gu, N.: 2022, EAST-Educational Adaptive-optics Solar Telescope. *Res. Astron. Astrophys.* **22**, 065003. DOI. ADS.

Rimmele, T., Marino, J.: 2006, The Evershed flow: Flow geometry and its temporal evolution. *Astrophys. J.* **646**, 593. DOI.

Scherrer, P.H., Bogart, R.S., Bush, R.I., Hoeksema, J.T., Kosovichev, A.G., Schou, J., Rosenberg, W., Springer, L., Tarbell, T.D., Title, A., Wolfson, C.J., Zayer, I., MDI Engineering Team: 1995, The solar oscillations investigation – Michelson Doppler imager. *Solar Phys.* **162**, 129. DOI. ADS.

Scherrer, P.H., Schou, J., Bush, R.I., Kosovichev, A.G., Bogart, R.S., Hoeksema, J.T., Liu, Y., Duvall, T.L., Zhao, J., Title, A.M., Schrijver, C.J., Tarbell, T.D., Tomczyk, S.: 2012, The Helioseismic and Magnetic Imager (HMI) Investigation for the Solar Dynamics Observatory (SDO). *Solar Phys.* **275**, 207. DOI. ADS.

Schmidt, W., von der Lühe, O., Volkmer, R., Denker, C., Solanki, S.K., Balthasar, H., Bello González, N., Berkefeld, T., Collados, M., Fischer, A., Halbgewachs, C., Heidecke, F., Hofmann, A., Kneer, F., Lagg, A., Nicklas, H., Popow, E., Puschmann, K.G., Schmidt, D., Sigwarth, M., Sobotka, M., Soltau, D., Staude, J., Strassmeier, K.G., Waldmann, T.A.: 2012, The 1.5 meter solar telescope GREGOR. *Astron. Nachr.* **333**, 796. DOI. ADS.

Schmidt, W., Bell, A., Halbgewachs, C., Heidecke, F., Kentischer, T.J., von der Lühe, O., Scheiffelen, T., Sigwarth, M.: 2014, A two-dimensional spectropolarimeter as a first-light instrument for the Daniel K. Inouye Solar Telescope. In: Ramsay, S.K., McLean, I.S., Takami, H. (eds.) *Ground-Based and Airborne Instrumentation for Astronomy V*, *Society of Photo-Optical Instrumentation Engineers (SPIE) Conference Series* **9147**, 91470E. DOI. ADS.

Yan, X., Li, Q., Chen, G., Xue, Z., Feng, L., Wang, J., Yang, L., Zhang, Y.: 2020, Dynamics evolution of a solar active-region filament from a quasi-static state to eruption: rolling motion, untwisting motion, material transfer, and chirality. *Astrophys. J.* **904**, 15. DOI. ADS.

Zhang, J.-C., Wang, X.-F., Mo, J., Xi, G.-B., Lin, J., Jiang, X.-J., Zhang, X.-M., Li, W.-X., Yan, S.-Y., Chen, Z.-H., Hu, L., Li, X., Lin, W.-L., Lin, H., Miao, C., Rui, L.-M., Sai, H.-N., Xiang, D.-F., Zhang, X.-H.: 2020, The Tsinghua University-Ma Huateng Telescopes for survey: overview and performance of the system. *Publ. Astron. Soc. Pac.* **132**, 125001. DOI. ADS.

Zhang, L., Bao, H., Rao, X., Guo, Y., Zhong, L., Ran, X., Yan, N., Yang, J., Wang, C., Zhou, J., Yang, Y., Long, Y., Fan, X., Feng, Z., Chen, D., Rao, C.: 2023, Ground-layer adaptive optics for the New Vacuum Solar Telescope: instrument description and first results. *Sci. China Phys. Mech. Astron.* **66**, 269611. DOI. ADS.

Publisher's Note Springer Nature remains neutral with regard to jurisdictional claims in published maps and institutional affiliations.

Springer Nature or its licensor (e.g. a society or other partner) holds exclusive rights to this article under a publishing agreement with the author(s) or other rightsholder(s); author self-archiving of the accepted manuscript version of this article is solely governed by the terms of such publishing agreement and applicable law.